

Broken Bar Fault Detection in IM Operating Under No-Load Condition

Dejan RELJIĆ, Dejan JERKAN, Darko MARČETIĆ, Djura OROS
 University of Novi Sad, Faculty of Technical Sciences, 21000 Novi Sad, Serbia
 reljic@uns.ac.rs

Abstract—This paper presents a novel method for broken rotor bar detection in a squirrel-cage induction motor (IM). The proposed method applies a single-phase AC voltage as a test signal on motor terminals, resulting in a stator backward-rotating magnetic field. The field ultimately causes additional current components in the stator windings whose magnitudes depend on the broken bar fault severity, even if the motor is unloaded. This allows robust broken bar fault detection based only on standard motor current signature analysis (MCSA) technique. The proposed fault detection method is at first verified via simulations, using an IM model based on finite element analysis (FEA) and multiple coupled circuit approach (MCCA). The subsequent experimental investigations have shown good agreement with both theoretical predictions and simulation results.

Index Terms—fault detection, current measurement, fast Fourier transform, induction motor, spectral analysis.

I. INTRODUCTION

Three-phase squirrel-cage induction motors (IMs) are the most widely used rotating electrical machines in modern industry. This is due to their numerous advantages.

In spite of their good characteristics, IMs are subjected to many electrical and mechanical faults. These faults are usually caused by various stresses acting upon the windings, rotor, bearings, and shaft [1-2]. The IM failure analysis in [2-3] has reported the most likely causes of failure. This paper is focused on the fault detection associated with broken rotor bars, due to its significance at the industrial level. Namely, broken rotor bars can lead to unwanted secondary effects: torque and speed oscillations that provoke premature wear of bearings, and rotor imbalance that causes high motor vibration and rotor eccentricity, due to which the rotor may rub against the stator. Moreover, healthy rotor bars in the vicinity of broken rotor bars are carrying additional current, leading to asymmetrical overheating in the rotor cage (Fig. 1). This causes rotor thermal bending and further fault propagation.

Due to the significance of the broken bar fault detection, numerous methods have been developed for the fault diagnosis. These methods can be invasive or non-invasive. Non-invasive techniques have become an industrial standard, because they allow the fault monitoring and detection without the need for costly and time-consuming motor disassembly and inspections. Various non-invasive techniques for broken rotor bar detection have been used: motor current signature analysis (MCSA) [4-10], search coil techniques for monitoring motor axial leakage flux [4], [11-

12], vibration measurement [13], or artificial intelligence based techniques [14-15]. Among them, the MCSA is the most often used [5]. The MCSA is based on the spectral analysis of stator currents. It can be performed using various digital signal processing techniques, measuring the stator currents in a steady state or during the transients [16].

The MCSA approach based on the fast Fourier transform (FFT) of the stator current signal is commonly used when the motor operates under steady-state condition. The main objective of the method is to detect fault-induced current components from the resultant spectrum of the current signal. The method is effective if the motor operates around the rated load condition.

However, the application of the steady-state MCSA has certain drawbacks. The method is inadequate under load fluctuations, which can be particularly troublesome in industrial applications. If the load varies during data acquisition, then the sideband frequencies change with the speed [17] and this can invalidate the MCSA process due to the smearing effect on the current spectrum [18]. Furthermore, mechanical power transmission elements can cause additional current components that can be misinterpreted as broken bar fault indicator [17]. Even still, the most important insufficiency of the method is the inability of fault diagnosis for light or no-load conditions. This is due to the fact that the rotor fault-induced current components are rather weak and can be masked by spectral leakage phenomena or/and affected by finite frequency resolution used [19]. To address this problem, it is suggested in [17] to shift the fundamental frequency to a DC component using the Hilbert transform, while the reduced stator current envelope method is used in [20] to separate the sideband frequencies from the fundamental one. Nevertheless, these methods require a long period of time for data acquisition, making them prone to speed and load variations, grid voltage and frequency deviations.

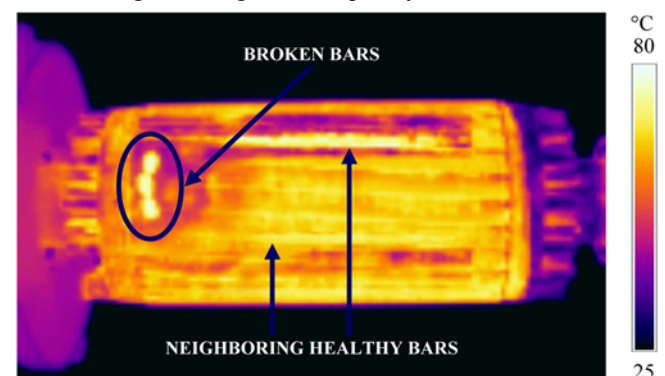


Figure 1. Thermal image of the faulty squirrel-cage rotor – three broken bars (left)

This work was supported by the Ministry of Education, Science and Technological Development of the Republic of Serbia under project III42004.

In order to overcome the disadvantages of the steady-state MCSA, another approach is to analyze the stator current signal spectra during transients, i.e. to perform the transient MCSA (TMCSA). The TMCSA is usually focused on the analysis of the startup current using short-time Fourier transform [5] or wavelet techniques [21-24]. Nevertheless, practical applications have shown that, if the motor startup time is too short, the detection of broken rotor bar cannot be performed [24]. Likewise, if the motor is started using a soft-starter, fault-induced components are affected by the harmonic content in the current.

In this paper, a novel method for broken rotor bars detection in a squirrel-cage IM is presented. The method presumes that the motor operates at the absolute no-load condition, keeping the motor shaft free. The broken bar detection procedure starts by applying a single-phase AC voltage on the motor terminals with all stator windings connected in series. Due to a single-phase power supply, a stator backward-rotating magnetic field is created. This field and rotor asymmetry, caused by broken rotor bars, creates components in the current spectra, which are employed as a fault indicator. These make the proposed method reliable and sensitive enough to detect broken rotor bars using the classical steady-state MCSA technique based on the FFT.

This rest of the paper is structured as follows. Section II outlines the theoretical basis for the broken bar related motor fault diagnosis. In Section III, the novel fault detection method is presented. Section IV gives the numerical model of the IM based on the multiple coupled circuit approach (MCCA). The simulation results are provided in section V, while the experimental verification is presented in Section VI. The simulation and experimental test results were obtained using the 11 kW, 400 V, 22 A, 50 Hz, four-pole, three-phase squirrel-cage IM and related parameters. Section VII provides the conclusion.

II. THEORETICAL BACKGROUND

A complete analysis of a three-phase IM with broken rotor bars, including experimental verification, can be found in [25]. In order to assist the reader in understanding the proposed novel method of broken bar fault detection, a brief explanation of the presence of broken bar sideband components in the stator current spectra is presented.

For the sake of simplicity, a two pole IM is considered, while speed will be expressed in terms of frequency. The results hold for a multipole machine, too. It is assumed that the stator windings are of ideal distribution. When these windings are supplied by balanced three-phase sinusoidal voltages a forward-rotating magnetic field in the air-gap occurs. This field rotates at synchronous speed, at the stator supply frequency f_s . Under assumption that the rotor cage is ideal, the slip-dependent electromotive forces (EMFs) induced in the rotor bars by the stator forward-rotating field are of equal amplitudes (but differ in phase) [25], and therefore currents in rotor bars are of equal amplitudes, too. The frequency of bar currents is $s \cdot f_s$, where s is the slip. If a breakage of rotor bars or end-ring occurs, bar currents will have different amplitudes and distribution [25], i.e. electrical asymmetry of the rotor cage appears. Such asymmetry is reflected in the rotor backward-rotating magnetic field. With respect to the stationary stator, this backward-rotating

magnetic field rotates at frequency f_{lsb} :

$$f_{lsb} = -s \cdot f_s + (1 - s) \cdot f_s = (1 - 2s) \cdot f_s. \quad (1)$$

As a result, EMFs of the frequency f_{lsb} are induced in the stator windings. Stator currents now consist not only of the fundamental component, but also of a component of the frequency f_{lsb} . This component is usually called the lower sideband (LSB) component around the fundamental. Due to a cyclic variation of currents, a torque pulsation at twice slip frequency ($2s f_s$) occurs, as well as speed oscillation, which is also a function of the drive inertia. This speed oscillation can reduce the magnitude of the LSB [18], but an upper sideband (USB) current component also appears in the stator windings due to rotor speed oscillation [26]. The frequency of the USB current component f_{usb} is [26]:

$$f_{usb} = (1 + 2s) \cdot f_s. \quad (2)$$

These are referred as classical twice slip frequency sidebands due to broken rotor bars [18] and it is generally assumed that these broken bar current sidebands are only caused by rotor asymmetry and rotor speed oscillation. Note that, due to imperfections of the construction, even healthy IMs always have some degree of rotor asymmetry.

Due to the interaction of broken bar sideband current components represented by frequencies (1) and (2) with flux and speed ripple, additional sideband current components occur at frequencies $(1 \pm 2ks) \cdot f_s$, where k is an integer (1,2,3,...).

III. THE NOVEL METHOD FOR BROKEN ROTOR BAR FAULT DETECTION

The previous section has provided the basic theoretical background for the formulation of the novel method for the broken rotor bar fault detection in the IM. The important property of the proposed method is that it introduces new sideband current components, which are clearly visible even at no-load and therefore can be used for more robust broken rotor bar fault detection.

The proposed method assumes that the three-phase squirrel-cage IM under test is decoupled from the load and runs freely at the rated voltage and rated frequency. Thereafter, motor terminals are disconnected from the main three-phase power source, followed by the reconnection of the stator windings in series connection (Fig. 2). Motor terminals (U1 and W1) are then supplied with an auxiliary single-phase power source. The motor continues to operate as a single-phase machine at reduced air-gap flux density. The principle of motor operation can be explained using the double revolving field theory.

Space-fundamental air-gap magnetomotive force (MMF) distribution F_{ag1} for the series motor windings connection (Fig. 2 b)) excited by a sinusoidally varying current in time leads to the following:

$$F_{ag1} = \frac{1}{2} F_{max} \cdot \left\{ \begin{aligned} &\cos(\omega_s t - \theta_e) + \cos(\omega_s t + \theta_e) + \\ &\sqrt{3} \sin(\omega_s t - \theta_e) - \sqrt{3} \sin(\omega_s t + \theta_e) \end{aligned} \right\}, \quad (3)$$

where F_{max} represents the amplitude of the space-fundamental MMF produced by the individual phases alone (depends on current amplitude and effective number of series turns per phase) [27], ω_s is the angular frequency of the applied excitation, and θ_e denotes the electrical space angle measured from the magnetic axis of the stator.

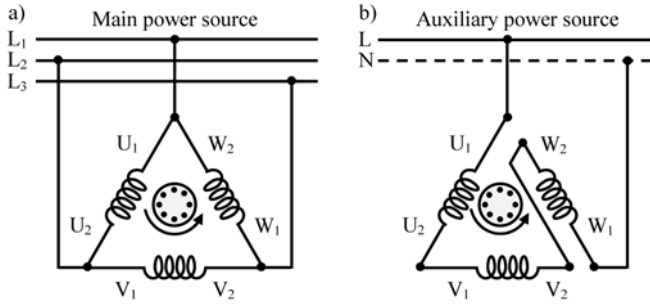


Figure 2. Reconnection of motor windings. a) Example of the delta windings configuration. b) Series windings configuration (the same principle is valid for the star connection)

The MMF distribution from (3) remains fixed in space with amplitude that varies sinusoidally at angular frequency ω_s , as illustrated in Fig. 3. The amplitude of the MMF is now $2F_{max}$, compared to $(3/2)F_{max}$ for the three-phase IM supplied with balanced three-phase voltages. This pulsating MMF can be resolved into two rotating MMF waves each of the amplitude of F_{max} with one traveling in the positive direction (anticlockwise) and other in the negative direction (clockwise), both with electrical angular velocity ω_s [27]. The positive-traveling magnetic field is actually forward-rotating magnetic field which produces useful torque T_f , while the negative-traveling magnetic field is backward-rotating field which produces torque in the opposite direction T_b , causing speed oscillation with the double frequency of the applied excitation. The resultant torque T can be obtained by summing these two torques and is illustrated in Fig. 4. The direction of motor rotation depends on the direction of torque provided by the previously three-phase operated IM. One can notice in Fig. 4 that, under ideal no-load condition, the rotor speed (ω_0) is lower in comparison to a three-phase operated IM. Due to the motor bearings friction and windage losses, no-load speed of the motor will be even lower, which is an important property of the single-phase motor operation for the proposed broken bar fault detection method.

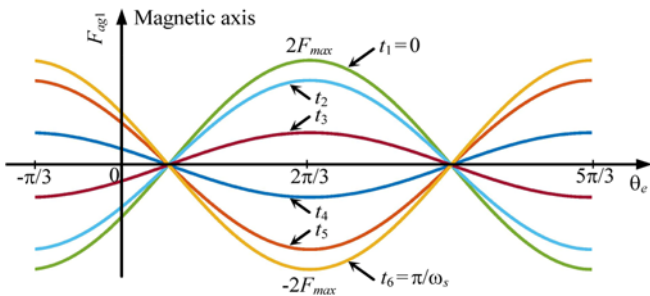


Figure 3. Space-fundamental air-gap MMF distribution from (3) at various times ($t_1 < t_2 < t_3 < t_4 < t_5 < t_6$) for the proposed windings connection

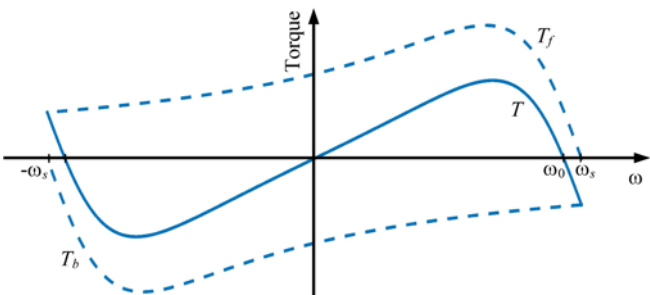


Figure 4. Illustration of torque-speed characteristics of the three-phase IM operating as a single phase machine with series motor windings connection

The interaction between the stator magnetic field and rotor bar currents (i.e. rotor forward- and backward-rotating magnetic fields) introduces new components in the stator current spectra. Due to a magnetic coupling between the stator phase a (or any other stator phase) and the rotor loop l , a part of the stator phase a flux linkage Ψ_{al} is:

$$\Psi_{al} = M_{al}(\theta_e) \cdot i_l(t), \quad (4)$$

where $M_{al}(\theta_e)$ represents stator-rotor mutual inductance between the stator phase a and the rotor loop l , and i_l is rotor loop current. If only the fundamental component of $M_{al}(\theta_e)$ is used, taking into account that M_{al} is the periodic function of θ_e , and considering that i_l has current components due to the rotor forward- and backward-rotating magnetic fields, the expression (4) can be further developed:

$$\Psi_{al} = M_{al} \cos(\theta_e) \cdot \left\{ \begin{array}{l} I_{lf} \cos(s\omega_s t) + \\ I_{lb} \cos((2-s)\omega_s t) \end{array} \right\}, \quad (5)$$

where I_{lf} and I_{lb} denote amplitudes of the rotor loop l current components (the so-called forward and backward currents). Note that, to avoid excessive complexity, initial phases in (5) are neglected. Taking into account rotor electrical speed ω instead of electrical space angle θ_e (including the speed oscillation of $\Delta\omega$ at the angular frequency of $2\omega_s$ caused by the stator backward-rotating field), the following is derived:

$$\Psi_{al} = \frac{1}{8} M_{al} \cdot \left\{ \begin{array}{l} 4I_{lb} \cos(\omega_s t) + \\ 4I_{lb} \cos((3-2s)\omega_s t) + \\ 4I_{lf} \cos(\omega_s t) + \\ 4I_{lf} \cos((1-2s)\omega_s t) + \\ (1/\omega_s)\Delta\omega I_{lb} \sin(\omega_s t) + \\ (1/\omega_s)\Delta\omega I_{lb} \sin((1-2s)\omega_s t) + \\ (1/\omega_s)\Delta\omega I_{lb} \sin(3\omega_s t) - \\ (1/\omega_s)\Delta\omega I_{lf} \sin(\omega_s t) - \\ (1/\omega_s)\Delta\omega I_{lf} \sin((1+2s)\omega_s t) + \\ (1/\omega_s)\Delta\omega I_{lf} \sin((3-2s)\omega_s t) + \\ (1/\omega_s)\Delta\omega I_{lf} \sin(3\omega_s t) + \\ (1/\omega_s)\Delta\omega I_{lb} \sin((5-2s)\omega_s t) \end{array} \right\}. \quad (6)$$

Similar expression to (6) can be obtained for other two stator windings, with only differences in the initial phases.

All the flux components in (6) induce corresponding currents at same angular frequencies, which makes a unique pattern in the current spectra. Although the expression (6) seems to be complex, only some spectra components are highly sensitive to the broken bar fault. Namely, the stator current component at the frequency of f_{lsbn} is the best candidate for reliable broken bar fault detection:

$$f_{lsbn} = (3-2s) \cdot f_s. \quad (7)$$

If rotor bar breakage occurs, then I_{lb} in (5) will increase, and consequently the second component of Ψ_{al} in (6) will also increase. Hence, stator current component at frequency represented by (7) is expected to increase, too. Furthermore, this current component will interact with stator flux and, due to additional torque variation and consequently speed oscillation, the current component of the following frequency f_{usbn} can also appear:

$$f_{usbn} = (3+2s) \cdot f_s. \quad (8)$$

These current components can be referred as LSB and USB components around the third harmonic of the fundamental frequency. In fact, sideband current components occur at

frequencies $(3 \pm 2ks)f_s$, where k is an integer $(1, 2, 3, \dots)$.

Standard broken bar fault indicators (1) and (2) can also be used. Other current components should be ignored (component $3f_s$ due to the possible harmonic pollution of the supply voltage, while the magnitude of the current component $(5-2s)f_s$ is small and it is therefore difficult to distinguish between healthy and faulty rotor cage).

IV. MCCA MODEL OF THE SQUIRREL-CAGE IM

In order to simulate broken rotor bar fault, a squirrel-cage IM model is developed. The model is based on the MCCA. This theory assumes that the stator and rotor of the IM consist of a group of coupled magnetic circuits.

The squirrel-cage rotor is represented by N_B equally spaced rotor loops (N_B is equal to the number of rotor bars), and two end rings. There are (N_B+1) independent current loops in the rotor cage. Rotor loops are coupled to each other and to the stator windings.

The voltage equations can be written as:

$$\mathbf{V} = \mathbf{R}\mathbf{I} + \frac{d}{dt}(\mathbf{L}\mathbf{I}), \quad (9)$$

where \mathbf{V} is voltage vector, \mathbf{I} is current vector, \mathbf{R} is resistance matrix, and \mathbf{L} is inductance matrix.

Voltage vector in (9) consists of stator \mathbf{V}_s and rotor \mathbf{V}_r voltage vectors:

$$\mathbf{V} = [\mathbf{V}_s \ \mathbf{V}_r]^T, \quad (10)$$

where

$$\mathbf{V}_s = [v_a \ v_b \ v_c] \wedge \mathbf{V}_r = [0 \ 0 \ \dots \ 0 \ 0]. \quad (11)$$

There are three stator voltages (v_a , v_b , and v_c) for three stator windings, and (N_B+1) rotor voltages equal to zero in (11).

Current vector \mathbf{I} in (9) consists of stator \mathbf{I}_s and rotor \mathbf{I}_r current vectors:

$$\mathbf{I} = [\mathbf{I}_s \ \mathbf{I}_r]^T, \quad (12)$$

where

$$\mathbf{I}_s = [i_a \ i_b \ i_c] \wedge \mathbf{I}_r = [i_{r1} \ i_{r2} \ \dots \ i_{rN_B} \ i_e]. \quad (13)$$

There are three currents in stator windings (i_a , i_b , and i_c), N_B rotor loops currents (denoted as $i_{r,k}$, $k=1, 2, \dots, N_B$) and one end-ring current (i_e) in (13).

Resistance matrix \mathbf{R} in (9) is a 2×2 diagonal matrix consisting of two matrices: stator resistance matrix \mathbf{R}_s which is a 3×3 diagonal matrix (consisting of stator windings resistances R_s), and rotor resistance matrix \mathbf{R}_r which is a $(N_B+1) \times (N_B+1)$ symmetrical matrix:

$$\mathbf{R} = \text{diag}(\mathbf{R}_s, \mathbf{R}_r), \quad (14)$$

$$\mathbf{R}_s = \text{diag}(R_s), \quad (15)$$

$$\mathbf{R}_r = \begin{bmatrix} R_{l1} & -R_{b2} & \dots & -R_{bN_B} & -R_{e1} \\ -R_{b1} & R_{l2} & \dots & 0 & -R_{e2} \\ \dots & \dots & \dots & \dots & \dots \\ 0 & 0 & \dots & -R_{bN_B} & -R_{e(N_B-1)} \\ -R_{b1} & 0 & \dots & R_{lN_B} & -R_{eN_B} \\ -R_{e1} & -R_{e2} & \dots & -R_{eN_B} & \sum_{i=1}^{N_B} R_{ei} \end{bmatrix}. \quad (16)$$

In (16) R_{lk} is rotor loop resistance ($1 \leq k \leq N_B$), defined as $R_{lk} = R_{bk} + R_{b(k+1)} + 2R_{ek}$, R_{bk} is bar k resistance, and R_{ek} is end-ring segment k resistance. For a healthy motor, the rotor loops are identical, but when a broken bar rotor fault occurs, some loops are affected. The numerical value of any

element in (16) can be chosen freely. Thus, computer simulations of fault caused by broken rotor bars can be easily performed.

Inductance matrix \mathbf{L} in (9) is composed of four matrices:

$$\mathbf{L} = \begin{bmatrix} \mathbf{L}_{ss} & \mathbf{L}_{sr} \\ \mathbf{L}_{rs} & \mathbf{L}_{rr} \end{bmatrix}. \quad (17)$$

Stator inductance matrix \mathbf{L}_{ss} is 3×3 and symmetrical, and it defines the magnetic coupling between stator windings (expressed with the self and mutual inductances, labeled as L and M , respectively). In this paper, \mathbf{L}_{ss} is considered to be a constant matrix:

$$\mathbf{L}_{ss} = \begin{bmatrix} L_a & M_{ab} & M_{ac} \\ M_{ba} & L_b & M_{bc} \\ M_{ca} & M_{cb} & L_c \end{bmatrix}. \quad (18)$$

Rotor inductance matrix \mathbf{L}_{rr} in (17) is a $(N_B+1) \times (N_B+1)$ symmetrical matrix. It defines the magnetic coupling of any rotor loop with all other rotor loops and the end-ring. It can be considered as a constant value matrix:

$$\mathbf{L}_{rr} = \begin{bmatrix} L_{l1} & \dots & M_{r1N_B} - L_{bN_B} & -L_{e1} \\ M_{r2N_B} - L_{b1} & \dots & M_{r2N_B} & -L_{e2} \\ \dots & \dots & \dots & \dots \\ M_{r(N_B-1)1} & \dots & M_{r(N_B-1)N_B} - L_{bN_B} & -L_{e(N_B-1)} \\ M_{rN_B1} - L_{b1} & \dots & L_{lN_B} & -L_{eN_B} \\ -L_{e1} & \dots & -L_{eN_B} & \sum_{i=1}^{N_B} L_{ei} \end{bmatrix}. \quad (19)$$

Rotor loop k inductance ($1 \leq k \leq N_B$) L_{lk} is defined as $L_{lk} = L_k + L_{bk} + L_{b(k+1)} + 2L_{ek}$, where L_k is loop k self-inductance, L_{bk} is rotor bar k leakage inductance, and L_{ek} is rotor end-ring segment k leakage inductance. Mutual inductances between arbitrary rotor loops m and n are labeled as $M_{r,mn}$ ($1 \leq m, n \leq N_B \wedge m \neq n$).

The rotor position-dependent stator-rotor matrix \mathbf{L}_{sr} in (17) is a $3 \times (N_B+1)$ matrix and it is defined as follows:

$$\mathbf{L}_{sr} = \begin{bmatrix} M_{al1}(\theta_e) & M_{al2}(\theta_e) & \dots & M_{alN_B}(\theta_e) & 0 \\ M_{bl1}(\theta_e) & M_{bl2}(\theta_e) & \dots & M_{blN_B}(\theta_e) & 0 \\ M_{cl1}(\theta_e) & M_{cl2}(\theta_e) & \dots & M_{clN_B}(\theta_e) & 0 \end{bmatrix}, \quad (20)$$

where $\mathbf{L}_{rs} = \mathbf{L}_{sr}^T$ holds. Mutual inductances between the stator windings and the rotor loop are labeled as $M_{x,lk}$, $x \in \{a, b, c\}$, $1 \leq k \leq N_B$. These mutual inductances are complex periodic functions of the electrical space angle θ_e (rotor angular position). In this paper they can be represented as pure cosine functions. Consecutive mutual inductances placed in the same row of the stator-rotor matrix have the phase shift of $2\pi/N_B$ electrical degrees. Last column in the stator-rotor inductance matrix has all zero values, because there are no significant couplings between stator windings and the rotor end ring. The iron core saturation effect is not included since this phenomenon is not of interest.

Each element of inductance matrices is determined using magneto-static 2-D FEA simulations [28], with the representation of inductances using Fourier series with a finite number of harmonics.

The proposed MCCA model of the IM is then modified with the objective to incorporate stator windings connected in series, supplied with a single-phase voltage. This is performed by summing stator flux linkages and substituting stator windings with one equivalent winding. Taking into consideration stator windings connection (Fig. 2 b)), stator

inductance matrix L_{ss} is:

$$L_{ss} = [3L - 2M], \quad (21)$$

where $L=L_a=L_b=L_c$, and $M=M_{ab}=M_{ba}=M_{bc}=M_{cb}=M_{ac}=M_{ca}$.

Likewise, the stator-rotor matrix L_{sr} will also change. It is now a $1 \times (N_B+1)$ matrix:

$$L_{sr} = \begin{bmatrix} M_{al1}(\theta_e) + M_{bl1}(\theta_e) - M_{cl1}(\theta_e) \\ M_{al2}(\theta_e) + M_{bl2}(\theta_e) - M_{cl2}(\theta_e) \\ \dots \\ M_{alN_B}(\theta_e) + M_{blN_B}(\theta_e) - M_{clN_B}(\theta_e) \\ 0 \end{bmatrix}^T. \quad (22)$$

The torque T acting on the rotor can be calculated as:

$$T = \frac{1}{2} p \begin{bmatrix} I_s \\ I_r \end{bmatrix}^T \left(\frac{d}{d\theta_e} \begin{bmatrix} L_{ss} & L_{sr} \\ L_{rs} & L_{rr} \end{bmatrix} \right) \begin{bmatrix} I_s \\ I_r \end{bmatrix}, \quad (23)$$

where p is the number of pole pairs.

Adding the equation of motion completes the model:

$$J \frac{d\omega_m}{dt} = T - T_l, \quad (24)$$

where J is the moment of inertia of the motor, ω_m is the mechanical angular speed of the motor, and T_l is the load torque. Since the motor is unloaded, T_l represents bearings friction and windage losses. For the particular case, they are modeled as a linear function of the motor speed.

V. RESULTS OF THE COMPUTER SIMULATIONS

In order to validate theoretical predictions of the proposed method for broken bars detection, this section presents the simulation results on the previously developed IM model. The proposed MCCA model was developed in Matlab/Simulink software. The IM parameters are obtained using the motor ratings provided in Section I. The results are shown in Fig. 5 and Fig. 6 in the form of the Fourier spectrum (using Hamming window) of the current signal.

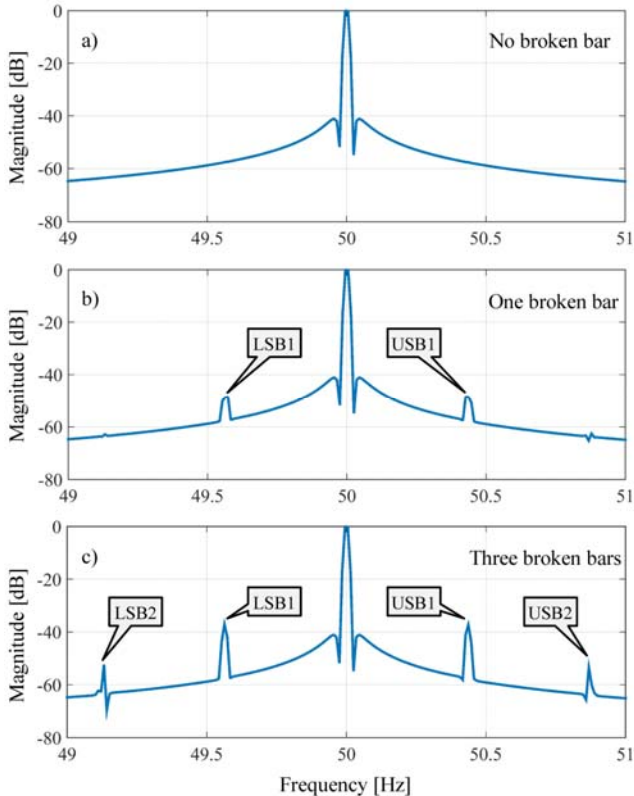


Figure 5. FFT motor current spectra around 50 Hz – simulation results

The results are obtained for a healthy rotor, a rotor with one and with three broken bars. Broken rotor bar fault was modeled by increasing the faulty bar resistance in (16). According to theoretical predictions and for the supply frequency of 50 Hz, sidebands around 50 Hz and 150 Hz should be considered. The motor operates at no-load, while the rotor speed is about 1494 rpm ($s=0.004$ p.u.). The sidebands $(1-2k)f_s$ and $(1+2k)f_s$ will be denoted as LSB k and USB k , respectively, while sideband components $(3-2k)f_s$ and $(3+2k)f_s$ will be labeled as LSB k _3F and USB k _3F, respectively, where k is an integer (1,2,3,...). The third harmonic current component will be marked as 3F.

For the healthy rotor, it is noticeable in Fig. 5 a) that only the fundamental current component of 50 Hz is clearly visible. Sideband components, predicted by the previously given theoretical analysis, cannot be seen due to the characteristics of the Hamming window. On the other hand, in Fig. 6 a), sideband current component at the frequency of about 149.6 Hz (marked as LSB1_3F) can be recognized. The magnitude of this component is about -61 dB. Moreover, in Fig. 6 a), current component at 150 Hz (marked as 3F) is also visible.

When a breakage of one rotor bar occurs, sidebands around the fundamental frequency (LSB1 and USB1 in Fig. 5 b)) become visible. These sidebands are located at frequencies of about 49.6 Hz (LSB1) and 50.4 Hz (USB1) with magnitudes of about -50 dB. By observing the sidebands around the third harmonic of the fundamental frequency (Fig. 6 b)), one can notice that the current component LSB1_3F has increased in magnitude to about -49 dB. The difference of the magnitude between the healthy rotor and the rotor with one broken bar is 11 dB. Additionally, the sideband component marked as LSB2_3F also appears in Fig. 6 b), as well as current component 3F.

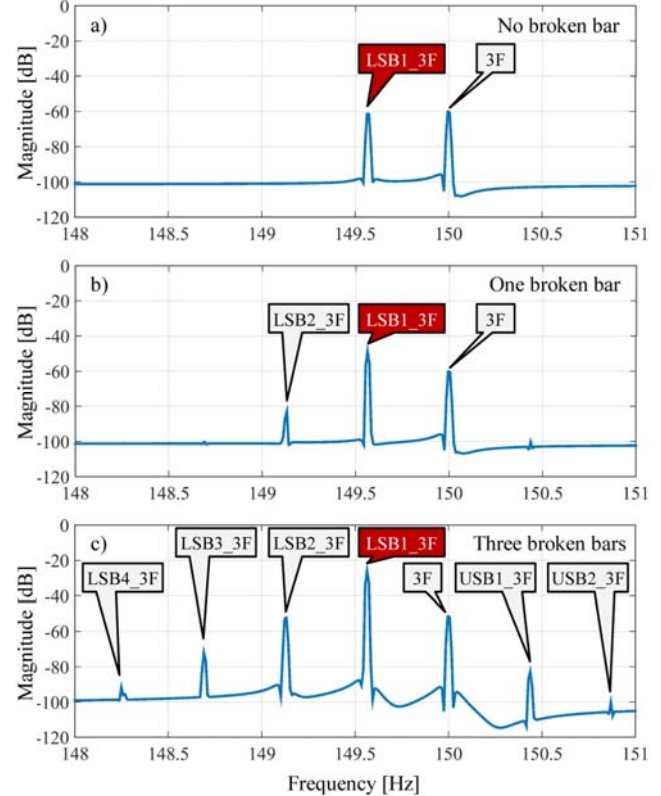


Figure 6. FFT motor current spectra around 150 Hz – simulation results

The third simulation was conducted on the IM model with three broken bars. The rotor fault characteristic frequency pattern is obvious in Fig. 5 c) and Fig. 6 c). Sideband components around the fundamental, LSB1 and LSB2 in Fig. 5 c), are increased in their magnitudes to about -37 dB. Besides, additional sideband components (LSB2 and USB2) occur. Similar results can be observed in Fig. 6 c). As shown, the sideband component around the third harmonic of the fundamental frequency LSB1_3F tends to grow with the fault severity. The magnitude of this current component is now about -25 dB. Compared to the healthy rotor cage, the magnitude of LSB1_3F is increased by 35 dB. This ensures a reliable broken bar fault detection. Due to a number of broken rotor bars, the magnitude of the current component marked as 3F is also increased. Moreover, additional sidebands (marked as LSB2_3F, LSB3_3F, LSB4_3F, USB1_3F, and USB2_3F) are noticeable.

VI. EXPERIMENTAL RESULTS

The performance of the proposed method was also validated experimentally using a three-phase squirrel-cage IM whose ratings are provided in Section I. A principle block diagram of the laboratory test bench, including the process of the MCSA for the broken bar fault detection procedure, is shown in Fig. 7, while the experimental time scheduler is shown in Fig. 8. Three identical rotors were used for the experimental tests (Fig. 9): rotor with healthy cage, rotor with one fully broken bar, and rotor with three fully broken bars. The same bearing types were used on all three rotors in order to eliminate their influences on the results.

The unloaded motor was initially supplied from the three-phase power supply at the rated voltage and frequency. After the successful completion of the starting process, the motor terminals were disconnected from the main power supply and then reconnected to the auxiliary single-phase power source at the rated frequency of 50 Hz. The terminal configuration switch (TCS in Fig. 7) performed this switching action, including the reconnection of motor windings in a series connection at the same time. The motor continued to run as a single-phase machine. Optical tachometer was used to determine motor speed, which was about 1494 rpm (ω_0 in Fig. 8), i.e. $s \approx 0.004$ p.u.

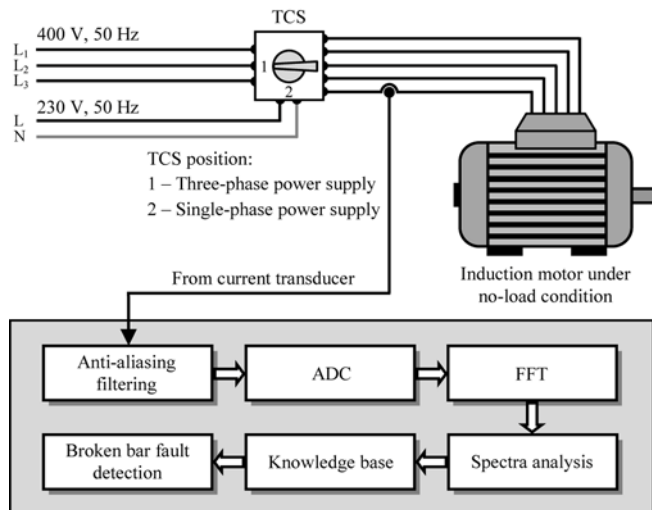


Figure 7. Block diagram of the laboratory test bench and the process of the MCSA for broken rotor bar fault detection

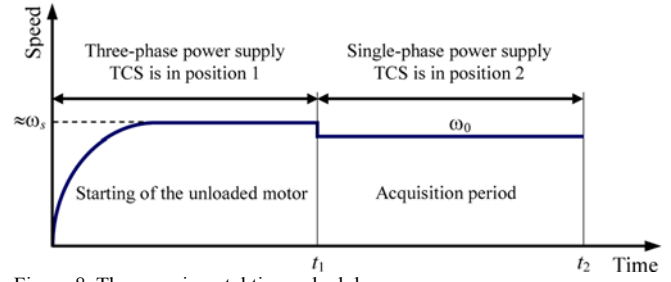


Figure 8. The experimental time scheduler



Figure 9. Healthy rotor and rotors with one and three fully broken bars

Data acquisition process was carried out during the motor single-phase operation (time period between t_1 and t_2 in Fig. 8) with the sampling interval of 100 μ s. Motor current was sensed by a Hall-effect current transducer. The phase current signal was then sent to the low-pass anti-aliasing filter. The filtered current signal was sampled at 12.8 kS/s by the 16-bit analog to digital converter (ADC), available at the NI USB-6251 high-speed data acquisition (DAQ) board. After the completion of the data acquisition process, the FFT was performed using the Hamming window function (due to the good relative sidelobe attenuation of -42.7 dB) to minimize the spectral leakage.

During the experimental tests, the motor current was low (approximately 1.8 Arms, which is only about 8% of the motor rated current), which is an additional benefit of the proposed method (low power auxiliary single-phase source is sufficient enough).

The FFT motor current averaged spectra in the case of a healthy rotor, a rotor with one broken bar, and a rotor with three broken bars are provided in Fig. 10 and Fig. 11. All current components are normalized to the fundamental current and expressed in dB.

The FFT current spectra obtained for the healthy rotor cage are shown in Fig. 10 a) and Fig. 11 a). As it can be seen in Fig. 10 a), there are no visible sideband current components. Only the fundamental current component is clearly visible. In Fig. 11 a), the current component marked as 3F can be observed. This current component is not only caused by the single-phase power supply, but also by the third order harmonic component of the power supply. However, more important are current sideband components marked as LSB1_3F and LSB2_3F, particularly LSB1_3F. The magnitude of the LSB1_3F is about -61 dB and this corresponds to the healthy rotor cage. Therefore, it can be used as a reference in the knowledge base block in Fig. 7 for the broken bar fault diagnosis. Current sideband LSB2_3F is created by the rotor asymmetry caused by imperfections of the rotor construction. The results are similar to those obtained by computer simulations, shown in Fig. 5 a) and Fig. 6 a).

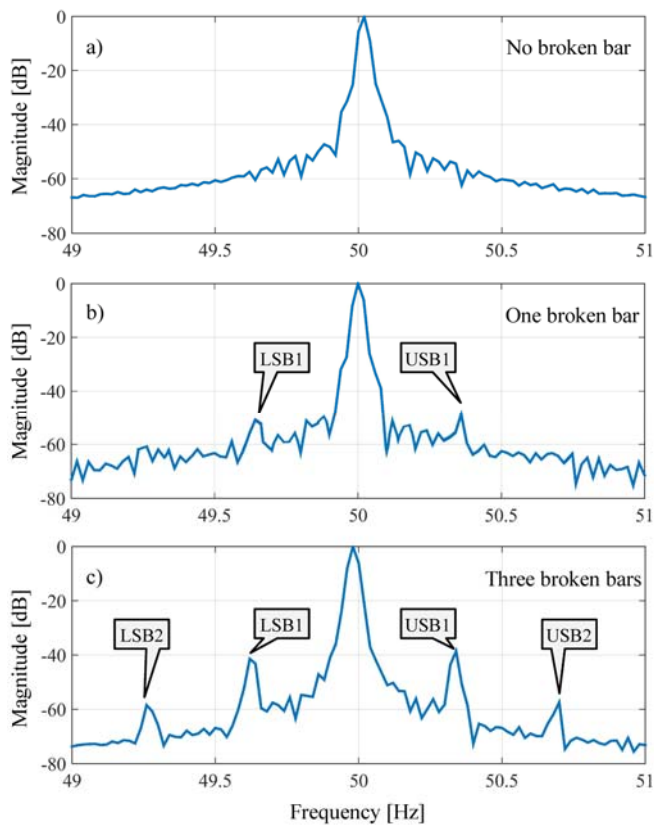


Figure 10. FFT motor current spectra around 50 Hz – experimental results

Current spectra in the case of one broken rotor bar are presented in Fig. 10 b) and Fig. 11 b). As indicated in Fig. 10 b), current sidebands around the fundamental frequency (LSB1 and USB1) appear, with magnitudes of about -50 dB (LSB1) and -48 dB (USB1). Similar can be observed in Fig. 11 b). Namely, the magnitude of the sideband current component LSB1_3F is increased to about -46 dB. Components LSB2_3F and 3F are also visible. This is in good agreement with the simulation results for the same type of fault, shown in Fig. 5 b) and Fig. 6 b).

Fig. 10 c) and Fig. 11 c) show the FFT current spectra which is the result of the third experiment, performed on the motor with three neighboring broken rotor bars. The magnitudes of the current components marked as LSB1 and USB1 in Fig. 10 c) are now even more visible: -41 dB for LSB1 and -38 dB for USB1. Sideband components LSB2 and USB2 are also visible. Similar results can be observed in Fig. 11 c). Magnitude of the current component marked as LSB1_3F is increased to about -27 dB. The difference of the magnitude of LSB1_3F between the healthy rotor and the rotor with three broken bar is 34 dB. Additional sidebands, marked as LSB2_3F, LSB3_3F, and USB1_3F are also noticeable. All these are in good agreement with the simulation results, shown in Fig. 5 c) and Fig. 6 c).

The results obtained from the experiments show that the current components related to the broken bar can be clearly recognized in the current spectra, thus confirming theoretical predictions and simulation results. Moreover, it can be easily observed from Fig. 11 that the magnitude of the current component LSB1_3F significantly increases with the increasing fault severity, i.e. the number of broken bars. As a result, this current component, together with components LSB1 and USB1 from Fig. 10, can be considered as a reliable broken bar fault indicator of the IM.

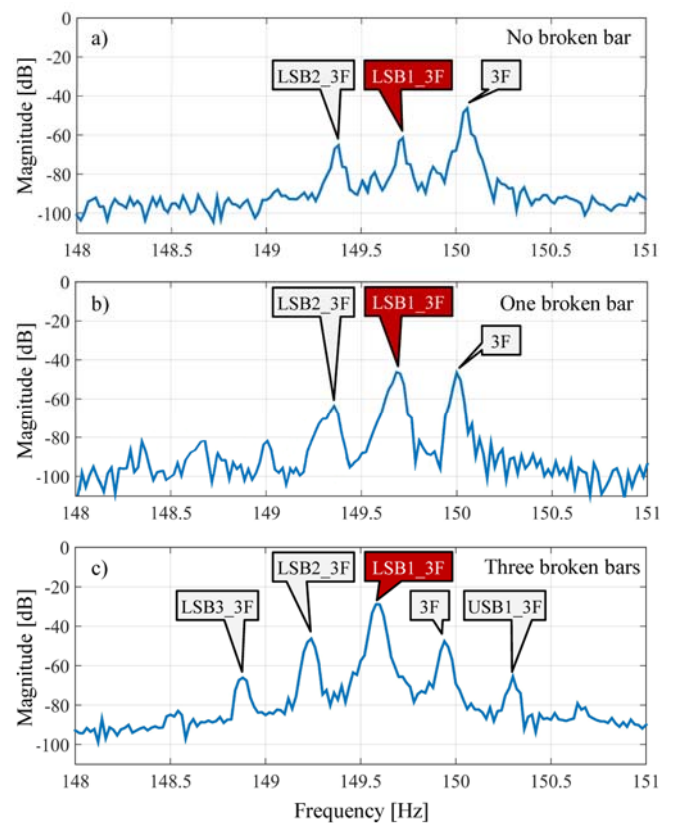


Figure 11. FFT motor current spectra around 150 Hz – experimental results

VII. CONCLUSION

The broken bar fault detection prevents more serious damage in the IM and therefore it is of great importance in industrial applications. Still, the existing fault detection techniques fail to detect the presence of broken rotor bars if the motor operates unloaded.

In this paper, the novel method for the broken bar fault detection of the three-phase squirrel-cage IM is proposed. In the contrast to conventional fault detection techniques, the method has been specifically developed to detect the broken rotor bar of the unloaded motor. For that reason, the application of the method is quite simple; it only requires the rearrangement of the motor windings and the use of the low-power single-phase power source. The usefulness of the proposed test setup is proven by the variety of computer simulations and experimental results. All the results confirm appearance of additional components in the current spectra, whose magnitudes can be used for the robust broken bar fault detection. Thus, the method enables a reliable and cost-effective broken bar fault detection of the unloaded IM.

REFERENCES

- [1] A. H. Bonnett, "Root Cause AC Motor Failure Analysis with a Focus on Shaft Failures," *IEEE Transactions on Industry Applications*, vol. 36, no. 5, pp. 1435-1448, Sep/Oct 2000. doi: 10.1109/28.871294
- [2] A. H. Bonnett, "Root cause failure analysis for AC Induction Motors in the petroleum and chemical industry," in *Proc. 57th Annu. Petroleum and Chemical Industry Conference*, San Antonio, 2010, pp. 1-13. doi: 10.1109/PCIC.2010.5666831
- [3] Olav Vaag Thorsen and Magnus Dalva, "A survey of Faults on Induction Motors in Offshore Oil Industry," *Petrochemical Industry, Gas Terminals, and Oil Refineries*, *IEEE Transactions on Industry Applications*, vol. 31, no. 5, pp. 1186-1196, Sep/Oct. 1995. doi: 10.1109/28.464536
- [4] G. B. Kliman, R. A. Koegl, J. Stein, R. D. Endicott, and M. W. Madden, "Noninvasive detection of broken rotor bars in operating

- induction motors,” *IEEE Trans. Energy Convers.*, vol. 3, no. 4, pp. 873–879, Dec. 1988. doi: 10.1109/60.9364
- [5] M. E. H. Benbouzid, “A review of induction motors signature analysis as a medium for faults detection,” *IEEE Transactions on Industrial Electronics*, vol. 47 no. 5, pp. 984-993, Oct. 2000. doi: 10.1109/41.873206
- [6] S. Nandi, H. A. Toliyat, and X. Li, “Condition monitoring and fault diagnosis of electrical motors—a review,” *IEEE Trans. Energy Convers.*, vol. 20, no. 4, pp. 719–729, Dec. 2005. doi: 10.1109/TEC.2005.847955
- [7] L. Mihet-Popa, “Current Signature Analysis as Diagnosis Media for Incipient Fault Detection,” *Advances in Electrical and Computer Engineering*, vol. 7, no. 2, pp. 11-15, November 2007. doi: 10.4316/AECE.2007.02003
- [8] G. Didier, E. Ternisien, O. Caspary, and H. Razik, “A new approach to detect broken rotor bars in induction machines by current spectrum analysis,” *Mech. Syst. Signal Process.*, vol. 21, no. 2, pp. 1127–1142, Feb. 2007. doi: 10.1016/j.ymssp.2006.03.002
- [9] K. N. Gyftakis and J. C. Kappatou, “The Zero-Sequence Current as a Generalized Diagnostic Mean in Δ -Connected Three-Phase Induction Motors,” *IEEE Trans. Energy Convers.*, vol. 29, no. 1, pp. 138–148, Mar. 2014. doi: 10.1109/TEC.2013.2292505
- [10] S. Shin, J. Kim, S. B. Lee, C. Lim, and E. J. Wiedenbrug, “Evaluation of the Influence of Rotor Magnetic Anisotropy on Condition Monitoring of Two-Pole Induction Motors,” *IEEE Transactions on Industry Applications*, vol. 51, no. 4, pp. 2896–2904, July 2015. doi: 10.1109/TIA.2015.2391432
- [11] A. Ceban, R. Pusca, and R. Romary, “Study of Rotor Faults in Induction Motors Using External Magnetic Field Analysis,” *IEEE Trans. Ind. Electron.*, vol. 59, no. 5, pp. 2082–2093, May 2012. doi: 10.1109/TIE.2011.2163285
- [12] S. W. Clark and D. Stevens, “Induction motor rotor bar damage evaluation with magnetic field analysis,” in *IEEE 10th International Symposium on Diagnostics for Electrical Machines, Power Electronics and Drives (SDMPED)*, Guarda, 2015, pp. 39–43. doi: 10.1109/DEMPED.2015.7303666
- [13] V. Climente-Alarcon, J. A. Antonino-Daviu, F. Vedreño-Santos, and R. Puche-Panadero, “Vibration Transient Detection of Broken Rotor Bars by PSH Sidebands,” *IEEE Trans. Ind. Appl.*, vol. 49, no. 6, pp. 2576–2582, Nov. 2013. doi: 10.1109/TIA.2013.2265872
- [14] S. Choi, E. Pazouki, J. Baek, and H. R. Bahrami, “Iterative Condition Monitoring and Fault Diagnosis Scheme of Electric Motor for Harsh Industrial Application,” *IEEE Trans. Ind. Electron.*, vol. 62, no. 3, pp. 1760–1769, Mar. 2015. doi: 10.1109/TIE.2014.2361112
- [15] S. Choi, B. Akin, M. M. Rahimian, and H. A. Toliyat, “Implementation of a Fault-Diagnosis Algorithm for Induction Machines Based on Advanced Digital-Signal-Processing Techniques,” *IEEE Trans. Ind. Electron.*, vol. 58, no. 3, pp. 937–948, Mar. 2011. doi: 10.1109/TIE.2010.2048837
- [16] M. Riera-Guasp, J. A. Antonino-Daviu, and G.-A. Capolino, “Advances in Electrical Machine, Power Electronic, and Drive Condition Monitoring and Fault Detection: State of the Art,” *IEEE Trans. Ind. Electron.*, vol. 62, no. 3, pp. 1746–1759, March 2015. doi: 10.1109/TIE.2014.2375853
- [17] R. Puche-Panadero, M. Pineda-Sanchez, M. Riera-Guasp, J. Roger-Folch, E. Hurtado-Perez, J. Perez-Cruz, “Improved Resolution of the MCSA Method Via Hilbert Transform, Enabling the Diagnosis of Rotor Asymmetries at Very Low Slip,” *IEEE Transactions on Energy Conversion*, vol. 24, no. 1, pp. 52–59, March 2009. doi: 10.1109/TEC.2008.2003207
- [18] W. T. Thomson and M. Fenger, “Current signature analysis to detect induction motor faults,” *IEEE Ind. Appl. Mag.*, vol. 7, no. 4, pp. 26–34, Jul./Aug. 2001. doi: 10.1109/2943.930988
- [19] M. C. Ian and R. Wendell, “Using current signature analysis technology to reliably detect cage winding defects in squirrel-cage induction motors,” *IEEE Trans. Ind. Appl.*, vol. 43, no. 2, pp. 422–428, Mar./Apr. 2007. doi: 10.1109/TIA.2006.889915
- [20] A. Sapena-Bano, M. Pineda-Sanchez, R. Puche-Panadero, J. Martinez-Roman, and Z. Kanovic, “Low-Cost Diagnosis of Rotor Asymmetries in Induction Machines Working at a Very Low Slip Using the Reduced Envelope of the Stator Current,” *IEEE Trans. Energy Convers.*, vol. 30, no. 4, pp. 1409–1419, Dec. 2015. doi: 10.1109/TEC.2015.2445216
- [21] M. Riera-Guasp, J. A. Antonino-Daviu, J. Roger-Folch, and M. P. M. Palomares, “The Use of the Wavelet Approximation Signal as a Tool for the Diagnosis of Rotor Bar Failures,” *IEEE Trans. Ind. Appl.*, vol. 44, no. 3, pp. 716–726, May 2008. doi: 10.1109/TIA.2008.921432
- [22] A. Bouzida, O. Touhami, R. Ibtouen, A. Belouchrani, M. Fadel, and A. Rezzoug, “Fault Diagnosis in Industrial Induction Machines Through Discrete Wavelet Transform,” *IEEE Trans. Ind. Electron.*, vol. 58, no. 9, pp. 4385–4395, September 2011. doi: 10.1109/TIE.2010.2095391
- [23] P. Karvelis, G. Georgoulas, I. P. Tsoumas, J. A. Antonino-Daviu, V. Climente-Alarcon, and C. D. Stylios, “A Symbolic Representation Approach for the Diagnosis of Broken Rotor Bars in Induction Motors,” *IEEE Trans. Ind. Inform.*, vol. 11, no. 5, pp. 1028–1037, Oct. 2015. doi: 10.1109/TII.2015.2463680
- [24] H. Douglas, P. Pillay, and A. K. Ziarani, “Broken Rotor Bar Detection in Induction Machines With Transient Operating Speeds,” *IEEE Transactions on Energy Conversion*, vol. 20, no. 1, pp. 135–141, March 2005. doi: 10.1109/TEC.2004.842394
- [25] S. Williamson, A. C. Smith, “Steady-state analysis of 3-phase cage motors with rotor-bar and end-ring faults,” *IEE Proceedings B - Electric Power Applications*, vol. 129, no. 3, pp. 93–100, May 1982. doi: 10.1049/ip-b.1982.0014
- [26] C. Hargis, B.G. Gaydon, and K. Kamish, “The detection of rotor defects in induction motors,” in *Proc. Institute Electrical Engineering EMDA Conf*, London, 1982, pp. 216–220.
- [27] A. E. Fitzgerald, C. Kingsley Jr., S. D. Umans. *Electric Machinery*. McGraw-Hill, pp. 173-244, 2005.
- [28] Dejan Jerkan and Darko Marčetić, “Advanced model of IM including rotor slot harmonics,” *COMPEL - Int. J. Comput. Math. Electr. Electron. Eng.*, vol. 34, no. 1, pp. 261–278, Jan. 2015. doi: <http://dx.doi.org/10.1108/COMPEL-03-2014-0051>